ELSEVIER

International Journal of Heat and Fluid Flow 23 (2002) 592–600

International Journal of HEAT AND FLUID FLOW

www.elsevier.com/locate/ijhff

Numerical study of momentum and heat transfer in unsteady impinging jets

Y.M. Chung [a,*], K.H. Luo [b], N.D. Sandham [c]

[a] *Department of Engineering, University of Warwick, Coventry CV4 7AL, UK*
[b] *Department of Engineering, Queen Mary, University of London, London E1 4NS, UK*
[c] *School of Engineering Sciences, University of Southampton, Southampton SO17 1BJ, UK*

Abstract

Direct numerical simulations of an unsteady impinging jet are performed to study momentum and heat transfer characteristics. The unsteady compressible Navier–Stokes equations are solved using a high-order finite difference method with non-reflecting boundary conditions. It is found that the impingement heat transfer is very unsteady and the unsteadiness is caused by the primary vortices emanating from the jet nozzle. These primary vortices dominate the impinging jet flow as they approach the wall. Detailed analysis of the instantaneous flow and temperature fields is performed, showing that the location of primary vortices significantly affects the stagnation Nusselt number. Spatio-temporal behaviour of the heat transfer is analysed, with instantaneous C_f and Nu variations showing the correlation between the local heat transfer and the flow field. Near the secondary vortices, the breakdown of the Reynolds analogy is observed.

Keywords: Numerical simulation; Impingement; Unsteady heat transfer; Jet

1. Introduction

Jet impingement has been encountered in many industrial and engineering applications. For example, the dynamics of impinging jets are important in developing vertical take-off and landing (VTOL) aircraft. Impinging jets have also been used as an effective method to enhance or suppress the heat transfer. In the metal sheet production process, impinging jets have been used to quench hot metal sheets from the furnace. Extensive reviews on impinging jets are available in Jambunathan et al. (1992), Martin (1977), Viskanta (1993), and Webb and Ma (1995).

Recently, jet impingement has been used for the cooling of electronic packages (Beitelmal et al., 2000; Lin et al., 1997). To avoid high hydrodynamic pressure caused by the impingement on the surface, low Reynolds number jets are often desirable. In electronics cooling, slot jets are preferred to circular jets. A slot jet has a wide impingement region and attains an almost isothermal condition on the surface. In contrast, a circular jet has a small impingement zone, restricting the effectiveness of cooling. Multiple circular jets are not as effective as slot jets due to the flow blockage between neighbouring jets.

Most previous studies on the impingement heat transfer have been concerned with high Reynolds number circular jets due to their wide industrial applications. Only a few experiments, beginning with Gardon and Akfirat (1966), are available on low Reynolds number impinging slot jets. Sparrow and Wong (1975) used the naphthalene sublimation technique to measure the mass transfer. The mass transfer results were converted to heat transfer coefficients by employing a heat–mass transfer analogy. Recently, a confined slot jet impingement experiment was performed by Lin et al. (1997) for electronic packages cooling applications. Jet impingement has also been studied numerically. The majority of those studies dealt with high Reynolds number flows with turbulence models (Behnia et al., 1999; Park and Sung, 2001). There are several numerical studies on low Reynolds number impinging jets (Al-Sanea, 1992; Chen et al., 2000; Chou and Hung, 1994; Law and Masliyah, 1984; Lee et al., 1997). However, all of the previous numerical studies are based on steady simulations. The unsteady characteristics of the impingement heat transfer are not yet fully understood (Liu and Sullivan, 1996; Özdemir and Whitelaw, 1992).

* Corresponding author. Tel.: +44-24-76-524-978; fax: +44-24-76-418-922.
E-mail address: y.m.chung@warwick.ac.uk (Y.M. Chung).

0142-727X/02/$ - see front matter
PII: S0142-727X(02)00155-8

Nomenclature

C_f	skin friction coefficient
D	jet width
e	internal energy per unit mass
E_t	total energy per unit mass
h	heat transfer coefficient
k	thermal conductivity
L_x	domain size in x direction
L_y	domain size in y direction
M	Mach number
Nu	Nusselt number, $Nu = hD/k$
p	static pressure
Pr	Prandtl number
q_i	heat flux vector
Re	Reynolds number, $Re = U_c D/\nu$
S_{ij}	strain rate, $S_{ij} = 0.5(\partial u_i/\partial x_j + \partial u_j/\partial x_i)$
St	Strouhal number, $St = fD/U_c$
T	temperature
u_i	velocity components
U_c	jet centerline velocity
x	lateral coordinate
y	normal to the wall coordinate
$\overline{\phi}$	time-mean value of ϕ
$\Delta(\phi)$	$(\phi - \overline{\phi})/\overline{\phi}$
γ	ratio of the specific heat
μ	dynamic viscosity
ν	kinematic viscosity
ρ	density
θ	inflow momentum thickness
τ_{ij}	shear stress tensor
ω	vorticity, $\omega = \mathrm{d}v/\mathrm{d}x - \mathrm{d}u/\mathrm{d}y$

Subscripts

c	jet centerline value
stag	stagnation point
v	primary vortices
w	wall value

In impinging jet flows, primary vortices emanate from the jet nozzle due to the shear layer instability (Jambunathan et al., 1992; Popiel and Trass, 1991). These primary vortices dominate the impinging jet flow as they approach the wall (Ho and Nosseir, 1981). In a previous study (Chung et al., 2001), it is found that the interaction of the primary vortices with the wall shear layer makes the impingement heat transfer strongly unsteady. For better understanding of jet impingement heat transfer, the unsteady heat transfer characteristics associated with the coherent flow structure are important. For electronics cooling applications, the unsteady heat transfer characteristics are as much important as the overall heat transfer efficiency.

In the present study, direct numerical simulations of an unsteady impinging jet at low Reynolds numbers are performed to study the unsteady impingement heat transfer. A high-order time-accurate finite difference method is used with non-reflecting boundary conditions (Jiang and Luo, 2000; Luo and Sandham, 1997). The instantaneous flow and temperature fields of an impinging jet are examined to investigate the correlation between the unsteady momentum and heat transfer. Preliminary results were presented by Chung et al. (2001).

2. Numerical method

2.1. Governing equations

The governing equations are the unsteady compressible Navier–Stokes equations using conservative variables (Chung et al., 2001; Jiang and Luo, 2000; Luo and Sandham, 1997).

$$\frac{\partial \rho}{\partial t} + \frac{\partial \rho u_i}{\partial x_i} = 0, \tag{1}$$

$$\frac{\partial \rho u_i}{\partial t} + \frac{\partial \rho u_i u_j}{\partial x_j} = -\frac{\partial p}{\partial x_j}\delta_{ij} + \frac{\partial \tau_{ij}}{\partial x_j}, \tag{2}$$

$$\frac{\partial E_t}{\partial t} + \frac{\partial E_t u_i}{\partial x_i} = -\frac{\partial p u_i}{\partial x_i} - \frac{\partial q_i}{\partial x_i} + \frac{\partial u_j \tau_{ij}}{\partial x_i}, \tag{3}$$

where ρ is the density, u_i are the velocity components, p is the thermodynamic pressure, E_t is the total energy density (internal + kinetic), τ_{ij} is the shear stress tensor, q_i is the heat flux vector and δ_{ij} is the Kronecker delta.

In this study, all the flow variables are non-dimensionalised by the jet centreline velocity U_c and the jet width D, and the resulting Reynolds number is $Re = U_c D/\nu$. A Cartesian coordinate system centred at the stagnation point on the impinging wall is used: x is the direction parallel to the impinging wall, and y is the negative jet direction (see Fig. 1). The corresponding lateral and axial velocities are u and v. A comprehensive description of the numerical method can be found in Luo and Sandham (1997) and Jiang and Luo (2000).

2.2. Boundary conditions

The mean velocity profile at the inflow is a top-hat profile with smooth edges. A hyperbolic tangent profile is used

$$U(x) = \frac{1}{2}\left[1 + \tanh\left(\frac{0.5 - |x|}{2\theta}\right)\right], \tag{4}$$

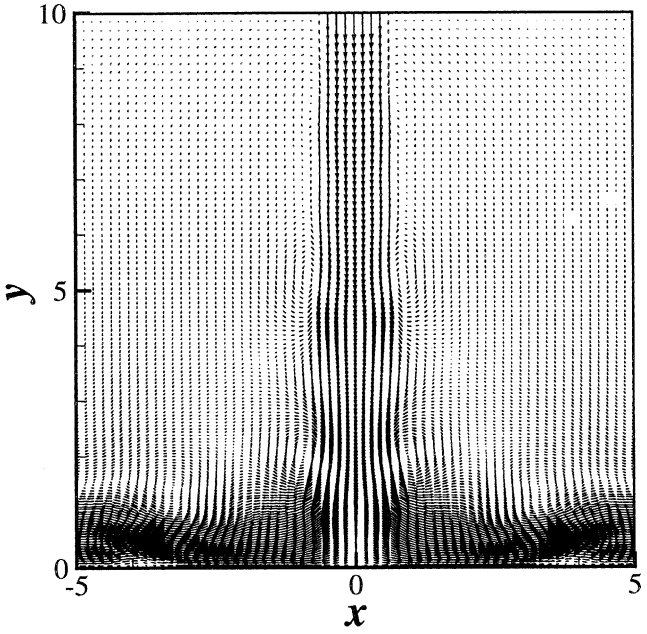

Fig. 1. Instantaneous velocity vectors of the impinging jet flow.

where θ is the inflow momentum thickness. The ratio of the jet width to the inflow momentum thickness is $D/\theta = 20$.

At the inflow boundary, the non-reflecting boundary condition of Poinsot and Lele (1992) is implemented, allowing the density to change in time. At the wall, the no-slip conditions are implemented (Poinsot and Lele, 1992). At the lateral exit, Thompson's (1987) non-reflecting boundary condition is applied. The isothermal boundary condition is imposed at the impinging wall. The ratio of the jet temperature to the impinging wall temperature is $T_j/T_w = 1.25$.

2.3. Numerical techniques

For spatial discretisation, a sixth-order finite-difference compact scheme developed by Lele (1992) is used in all directions. The spatially discretised governing equations are advanced in time explicitly with a low storage third-order Runge–Kutta method (Williamson, 1980). After both flow and thermal field have reached a quasi-steady state, the averages over time are taken.

A grid refinement study was performed until more grid points do not cause any significant differences in the result. A hyperbolic sine function, sinh, is used to give local grid refinement in the wall layer.

$$y(\eta) = L_y \frac{\sinh(b_y \eta)}{\sinh b_y}, \quad 0 \leqslant \eta \leqslant 1, \tag{5}$$

where $b_y = 2.0$ is a grid control parameter. A computational grid up to 384×384 is used in the simulation. It is noted that the grid points used in this study are much larger than those used in previous numerical studies (Al-Sanea, 1992; Chen et al., 2000; Chou and Hung, 1994; Law and Masliyah, 1984; Lee et al., 1997).

The time step is determined by a CFL-criterion, derived from a numerical stability analysis. The theoretical value for stability is $\mathrm{CFL} = \sqrt{3}$. The final value of the CFL number is determined by numerical stability tests, in which the CFL number is systematically reduced until a further reduction is unnecessary. The time histories of wall temperatures show identical results to those using half of the time steps.

3. Results and discussion

Fig. 1 shows instantaneous velocity vectors of the impinging jet flow together with the definition of the relevant coordinates. The computational domain size of interest is $[-L_x, L_x]$, and $[0, L_y]$ in the x and y directions, respectively, where $L_x = 5$ and $L_y = 10$. This value of L_y is larger than the extent of the potential core of the slot jet (Chung et al., 2001; Gauntner et al., 1970; Livingood and Hrycak, 1973). The jet comes from the top and the impinging wall is located at $y = 0$. The primary vortices emanating from the jet shear layer are clearly seen, which is the characteristic of unsteady jet flow. As the flow is deflected from the impinging wall, a wall jet is developed. The interaction of the primary vortices with the wall shear layer gives rise to unsteady vortical motions.

3.1. Stagnation Nusselt number

Simulations are performed at three Reynolds numbers, $Re = 300$, 500 and 1000. The numerical parameters used in the present study are given in Table 1. The time-mean stagnation Nusselt number $\overline{Nu}_{\mathrm{stag}}$ (where $\overline{(\ )}$ represents the time-mean value) increases with the Reynolds number and the present simulation can be well correlated with the boundary-layer theory, $\overline{Nu}_{\mathrm{stag}} \sim Re^{0.5}$. The Nusselt number distribution for $Re = 500$ compares well with the experimental data of Sparrow and Wong (1975) and the result is shown in Fig. 2. Sparrow and Wong (1975) used the naphthalene sublimation technique to measure the mass transfer. The mass transfer results were converted to heat transfer coefficients by employing a heat–mass transfer analogy. It should be noted that the Reynolds number in the

Table 1
Parameters of impinging jet simulations

Case	Re	L_x	L_y	Mesh sizes
Case 1	300	5	10	256^2
Case 2	500	5	10	300^2
Case 3	1000	5	10	384^2

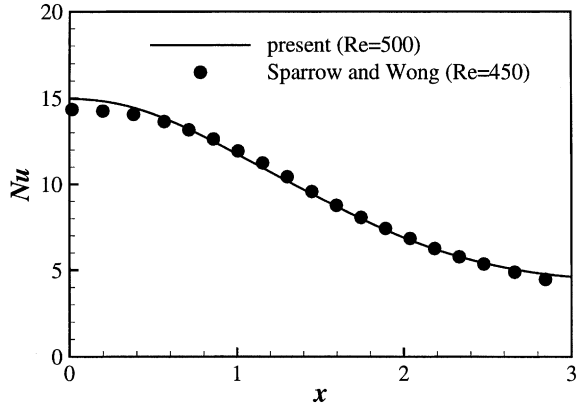

Fig. 2. Comparison with experimental data at $Re = 500$. Symbols are the experimental data of Sparrow and Wong (1975) at $Re = 450$.

experiment is $Re = 450$. Fig. 2 shows good agreement in the impingement region.

The time history of the stagnation Nusselt number Nu_{stag} is shown in Fig. 3 for the three cases. Nusselt number is defined as $Nu = hD/k$, where h is the heat transfer coefficient $h = k(\mathrm{d}T/\mathrm{d}y)/(T_j - T_{\mathrm{w}})$ and k is the thermal conductivity of the fluid. Nu_{stag} shows unsteady and oscillating behaviour. The fluctuations in the Nusselt number increase with the Reynolds number and at $Re = 500$ the oscillating behaviour of heat transfer begins to show. This is due to the direct influence of the coherent vortical structure of the impinging jet (see Fig. 4). In this simulation, no forcing is imposed at the inflow and the jet develops in a varicose (symmetric) mode near the jet nozzle. For higher Reynolds numbers ($Re = 1000$), the periodicity of the Nusselt number is not clear. This is partly due to the fact that the jet flow at $Re = 1000$ also has a weak sinuous (asymmetric) mode as well as the varicose mode. It is found that in the present study the dominant frequency corresponds to a Strouhal number of $St \approx 0.2$, based on U_{c} and D. This value falls within the range of other experimental (Didden and Ho, 1985; Ho and Huerre, 1984) and numerical (Hoffmann and Benocci, 1994; Olsson and Fuchs, 1998) results.

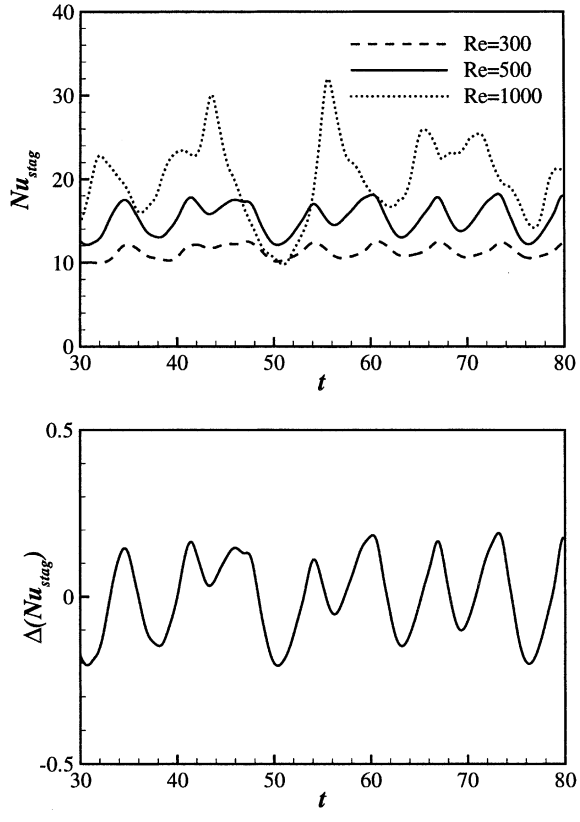

Fig. 3. Time history of the stagnation Nusselt number: (a) Nu_{stag} and (b) $\Delta(Nu_{\mathrm{stag}})$ for $Re = 500$.

Changes in the instantaneous stagnation Nusselt number $\Delta(Nu_{\mathrm{stag}})$ is shown in Fig. 3(b) for $Re = 500$. Here, $\Delta(Nu_{\mathrm{stag}})$ indicates the ratio of the stagnation Nusselt number to its time-mean value

$$\Delta(Nu_{\mathrm{stag}}) = \frac{Nu_{\mathrm{stag}} - \overline{Nu}_{\mathrm{stag}}}{\overline{Nu}_{\mathrm{stag}}}. \tag{6}$$

The oscillation amplitude of the instantaneous Nusselt number is about 20% of $\overline{Nu}_{\mathrm{stag}}$.

3.2. Correlation between flow and temperature fields

To investigate the unsteady impingement heat transfer, the flow field of $Re = 500$ is analysed in detail. Fig. 4 shows instantaneous temperature and vorticity contour lines at two time instants. The Nusselt number distribution along the wall is also presented in the figure. Two time instants are carefully chosen such that P1 represents the time instant when the instantaneous stagnation Nusselt number Nu_{stag} has a local maximum and P3 indicates the time instant for a local minimum of Nu_{stag}. In the figure, the primary vortices close to the impinging wall are denoted by PV, where NV represents the next primary vortices emanating from the jet shear layer and SV indicates the secondary vortices near the wall.

It is clear that the flow and temperature fields are closely related with each other. At P1 where Nu_{stag} has a local maximum (Fig. 4(a)), the primary vortex PV locates very close to the wall. The proximity of the strong primary vortex results in a thin thermal boundary layer at the stagnation region. As the primary vortex PV moves downstream, Nu_{stag} decreases due to the thickening of the thermal boundary layer. As PV moves further downstream with the new primary vortex NV not yet affecting the dynamics near the impinging wall directly, Nu_{stag} keeps decreasing and has a minimum at P3 (Fig. 4(b)). As NV approaches the wall, Nu_{stag} begins to increase again and completes the cycle (see also Fig. 8).

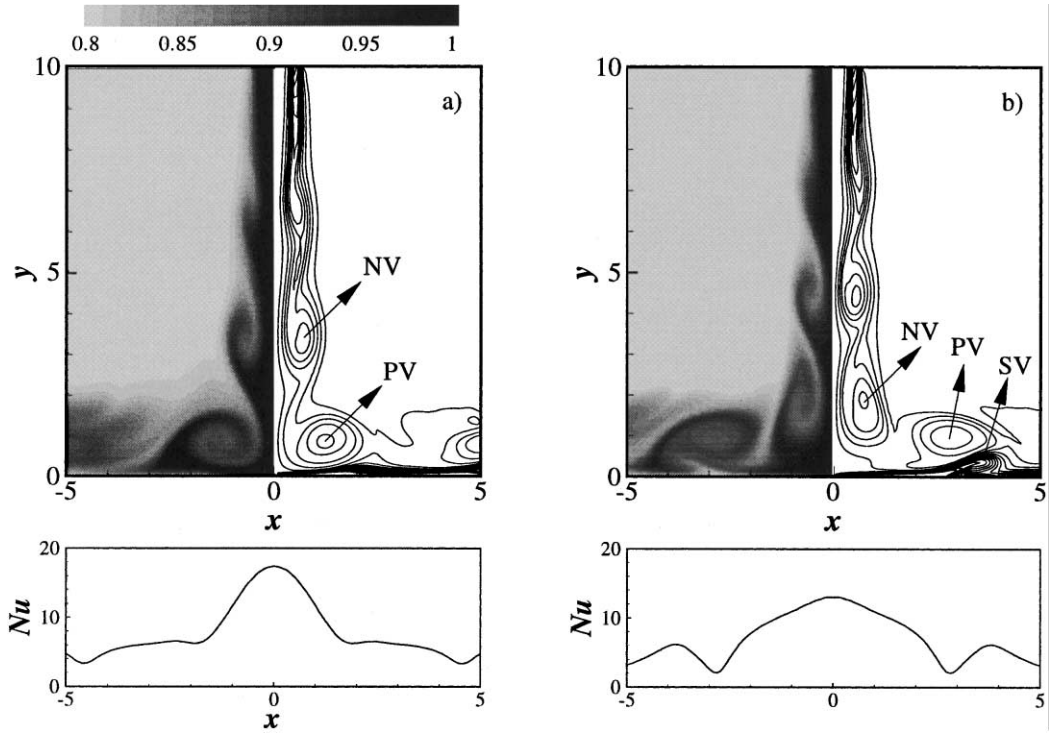

Fig. 4. Temperature (left) and vorticity (right) field contours and Nusselt number distributions (bottom) at several time instants for $Re = 500$, at (a) P1, (b) P3.

As the flow goes downstream, the wall jet separates due to the interaction between the primary vortices and the wall, and consequently secondary vortices are formed. These secondary vortices are responsible for the secondary maximum in *Nu*. The secondary peak in the transfer coefficient was observed when the flow has strong vortices (Law and Masliyah, 1984; Meola et al., 1996). The secondary vortices SV move downstream together with the primary vortex PV. Upstream of the secondary vortices, *Nu* has a local minimum (see later).

It has been found that the primary vortices play an important role in unsteady impingement heat transfer (Liu and Sullivan, 1996). It is expected that the strength and location of the vortices correlate well with the stagnation Nusselt number. Unsteady vorticity fields for $Re = 300$ and 500 are analysed. The following correlation is found to match very well and the result is shown in Fig. 5.

$$Nu_{\mathrm{stag}} \sim \frac{(\omega_{\max}/\nu)^{1/2}}{y_{\mathrm{v}}}, \tag{7}$$

where $\omega_{\max}$ is the maximum value of the primary vortices ($\omega = \mathrm{d}v/\mathrm{d}x - \mathrm{d}u/\mathrm{d}y$), and y_{v} is their location. The strength of the vortex is weakened due to the viscous effects but the decrease is only 10% of the strength (Chung et al., 2001). It is found that the modulation of the instantaneous Nusselt number is attributed mainly to the location of the primary vortices rather than their strength. The location of the primary vortices are shown in Fig. 6. It is noted that Orlandi and Jiménez (1994) suggested a similar correlation for the unsteady skin friction in the presence of streamwise vortices.

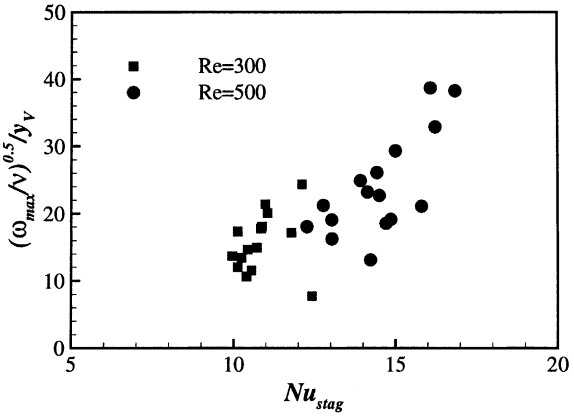

Fig. 5. Correlations between the stagnation Nusselt number and the vorticity field, $\sqrt{\omega_{\max}/\nu}/y_{\mathrm{v}}$ vs. Nu_{stag}.

3.3. Instantaneous C_{f} and Nu distributions

The oscillatory behaviour of the *Nu* distribution is clearly seen in Fig. 7, which shows space–time plots of *Nu* for $Re = 500$ and 1000. The downstream movements of the maximum and minimum *Nu* are clear. At $Re = 500$ the patterns are quite regular although they are not exactly periodic in time. The stagnation Nusselt

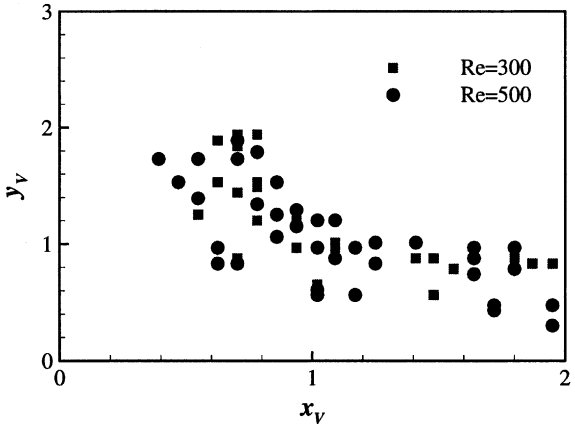

Fig. 6. The locations of primary vortices.

number is oscillatory as shown in Fig. 3. It is clear that the oscillatory behaviour remains as the flow goes downstream. As expected from Fig. 3, the patterns for $Re = 1000$ become a little irregular although oscillatory heat transfer characteristics are still seen. The analysis is focused on the $Re = 500$ case.

The friction coefficient (C_f) and the Nusselt number (Nu) distributions at several time instants are shown in Fig. 8 for $Re = 500$. P1 and P3 are the same instants shown in Fig. 4. P2 and P4 correspond to the temperature-decreasing and temperature-increasing phases, respectively. C_f has a maximum near $x = 1$ where the primary vortices impinge on the wall. The magnitude and location of the C_f maximum vary in time as the primary vortices move downstream. For the trajectories of the primary vortices, see Fig. 6. The locations of the minimum C_f values also move downstream. At P2, the minimum C_f value is almost zero at $x = 2.5$, resulting in the minimum in Nu at a slightly upstream location ($x = 2.2$). At P3, the minimum C_f value becomes negative due to the secondary vortices as shown in Fig. 4(b).

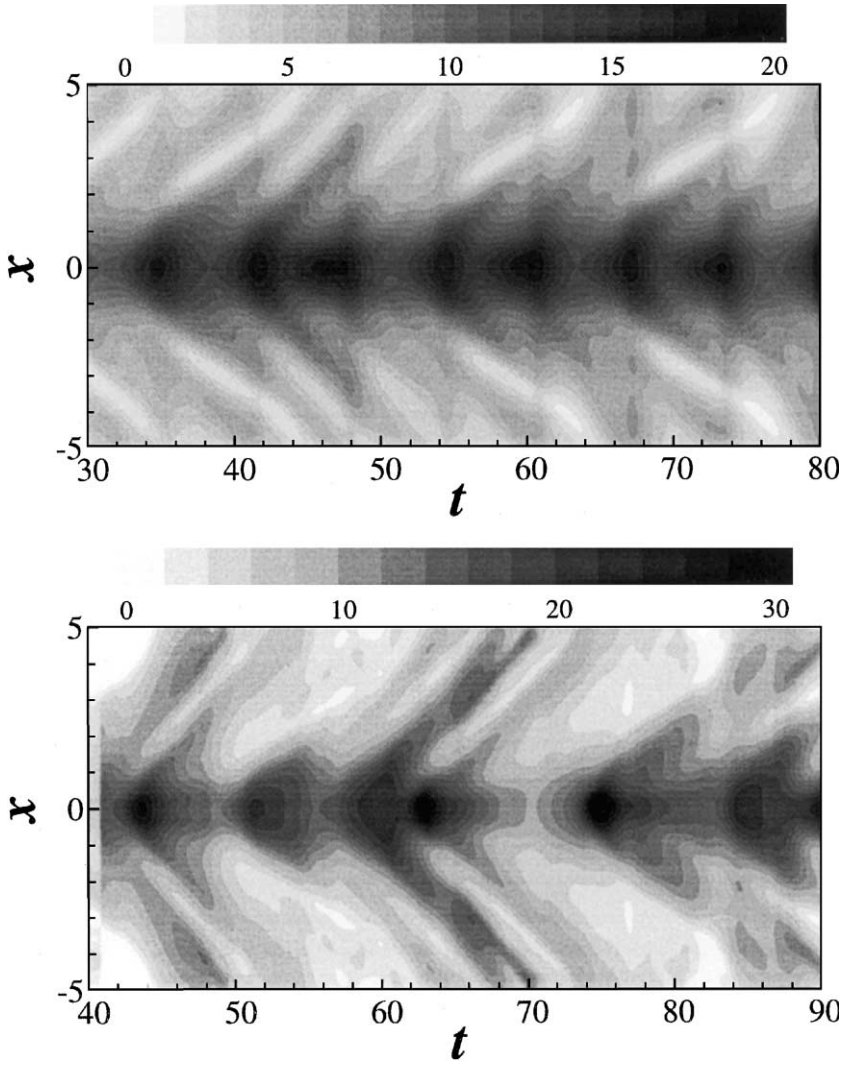

Fig. 7. Space–time contour plots of Nu: (a) $Re = 500$ and (b) $Re = 1000$.

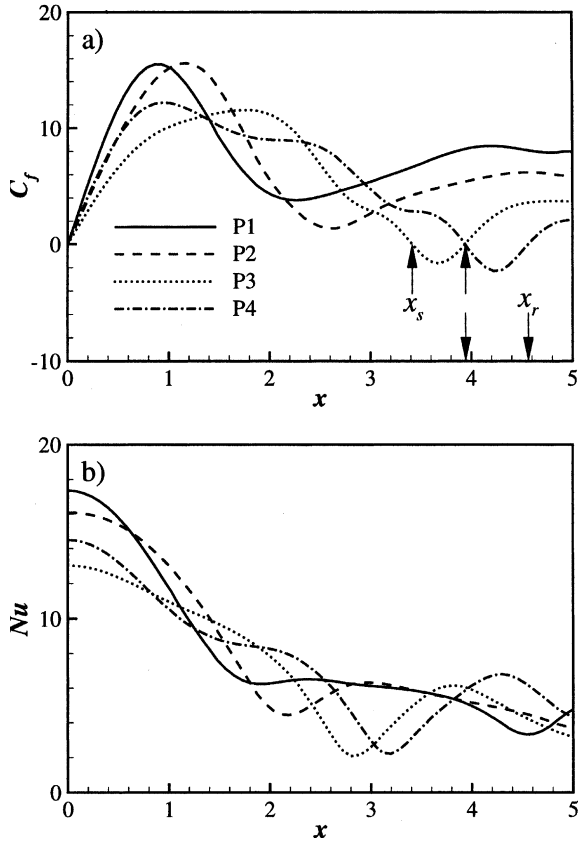

Fig. 8. C_f and Nu variations at several time instants for $Re = 500$: (a) C_f and (b) Nu. ↑ indicates the separation points, x_s, and ↓ the reattachment points, x_r.

The locations of flow separation (x_s) and reattachment (x_r) for P3 and P4 are indicated as arrows in the figure. x_s is 3.41 and 3.94 and x_r is 3.94 and 4.56 for P3 and P4, respectively. The secondary maximum Nusselt number occurs between x_s and x_r at 3.83 for P3 and 4.30 for P4. The local Nusselt number has a secondary maximum underneath the secondary vortex (Law and Masliyah, 1984; Meola et al., 1996). A little upstream of x_s, the Nusselt number has a local minimum due to the thickening of the thermal boundary layer.

3.4. The Reynolds analogy

To understand the unsteady heat transfer characteristics, the Reynolds analogy between unsteady momentum and energy transfer is investigated. Reynolds (1874) first suggested proportionality between fluid friction and heat flux. In many convective heat transfer studies, the Reynolds analogy has been successfully applied (Cebeci, 1973; Gaviglio, 1987; Reynolds, 1975). However, the breakdown of the Reynolds analogy has also been observed by Huang et al. (1995) and Bae and Sung (2001). Although the Reynolds analogy has been used based on the time-mean transport of momentum and heat, recent unsteady Reynolds-averaged Navier–Stokes (URANS) studies apply the Reynolds analogy implicitly (Tucker, 2001). The turbulent Prandtl number Pr_t has been taken as a constant. It is worthwhile examining the Reynolds analogy in the presence of large-scale unsteady vortical motions.

Fig. 9 gives the $\Delta(C_f)$ and $\Delta(Nu)$ distributions at several time instants, where $\Delta(C_f) = (C_f - \overline{C_f})/\overline{C_f}$ and $\Delta(Nu) = (Nu - \overline{Nu})/\overline{Nu}$. Both distributions change significantly in the downstream (x) direction. Near the stagnation point ($x \leqslant 1$), the changes in $\Delta(C_f)$ and $\Delta(Nu)$ are quite similar to each other. Further downstream, however, the $\Delta(C_f)$ distributions move downstream faster than those of $\Delta(Nu)$. This feature is clear from the location of local minima. At P1 and P2, minima of $\Delta(C_f)$ occur at $x = 2.0$ and 2.6, respectively, while $\Delta(Nu)$ has minima at $x = 1.7$ and 2.1. Based on the Reynolds analogy, $\Delta(C_f)$ and $\Delta(Nu)$ should be equal each other, i.e., $\Delta(C_f) = \Delta(Nu)$. However, from the figure it is clear that the Reynolds analogy cannot be adopted in this case. Especially, near the secondary vortices (see P3 and P4), the breakdown of the Reynolds analogy is clear. For example, the distributions at $x = 3$ show the complete breakdown of the Reynolds analogy.

Fig. 10 shows the time variations of $\Delta(C_f)$ and $\Delta(Nu)$. Two measuring locations are selected from Fig. 9: $x = 1$

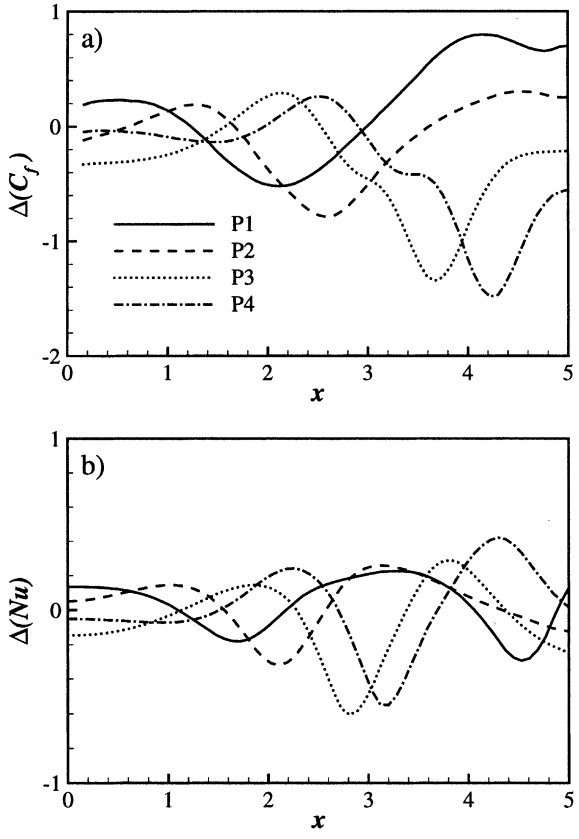

Fig. 9. $\Delta(C_f)$ and $\Delta(Nu)$ variations at several time instants for $Re = 500$: (a) $\Delta(C_f)$ and (b) $\Delta(Nu)$.

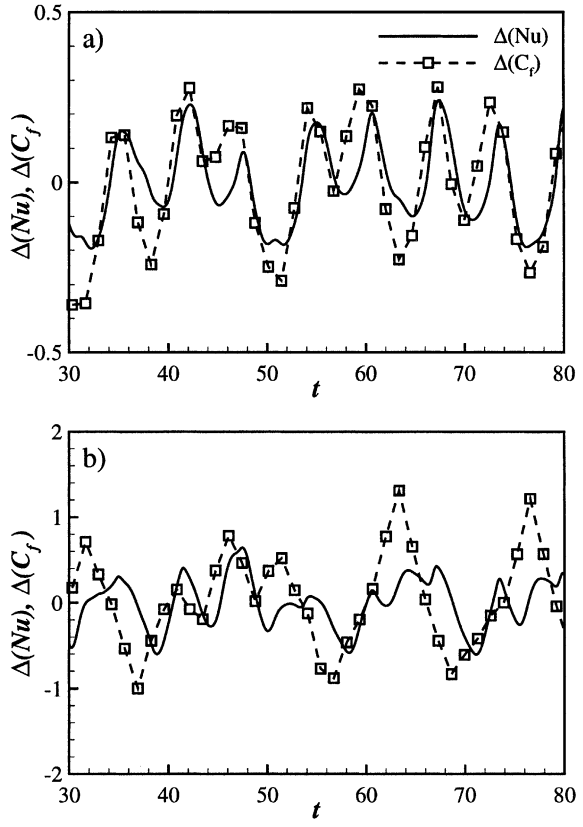

Fig. 10. Time histories of temperature and velocity gradients for $Re = 500$: (a) $x = 1$ and (b) $x = 3$.

and 3. Both distributions show oscillatory behaviour similar to Fig 3. At $x = 1$ the patterns of $\Delta(C_f)$ and $\Delta(Nu)$ are quite similar although magnitudes differ significantly. The deviation between $\Delta(C_f)$ and $\Delta(Nu)$ is more evident as the flow goes further downstream. At $x = 3$, $\Delta(C_f)$ and $\Delta(Nu)$ do not follow each other and the complete breakdown of the Reynolds analogy is seen. This feature is attributed to the secondary vortices near the wall and consistent with the findings from Fig. 8.

4. Concluding remarks

Direct numerical simulations have been performed to study unsteady impingement heat transfer. A high-order time-accurate finite-difference scheme was used to solve unsteady compressible Navier–Stokes and energy equations. It was found that the impingement heat transfer is very unsteady and oscillatory in time. At the stagnation point, the amplitude of the oscillation is as high as 20% of the time-mean value. The analysis shows that the unsteadiness of the impingement heat transfer is mainly caused by the primary vortices emanating from the jet nozzle. These primary vortices dominate the impinging jet flow as they approach the wall. It is clear from the space–time contour plots of Nu that the interaction of the primary vortices with the wall shear layer makes the impingement heat transfer strongly unsteady. The correlation between the local heat transfer and the flow field is examined. The strength and location of the primary vortices influence the stagnation Nusselt number. It is found that the vortex location has a much stronger effect on Nu_{stag} than the vortex strength. Instantaneous C_f and Nu variations show that local heat transfer distributions correlate closely with the flow fields. The Reynolds analogy is examined using instantaneous flow and temperature fields. In the presence of large-scale unsteady vortical motions, the breakdown of the Reynolds analogy is observed.

Acknowledgements

The support of the Engineering and Physical Sciences Research Council (EPSRC) of the United Kingdom under grant number GR/L56237 is gratefully acknowledged. Supercomputer resources were provided by EPSRC under grant number GR/M08424.

References

Al-Sanea, S., 1992. A numerical study of the flow and heat-transfer characteristics of an impinging laminar slot-jet including crossflow effects. Int. J. Heat Mass Trans. 35 (10), 2501–2513.

Bae, S., Sung, H.J., 2001. Breakdown of the Reynolds analogy in a stagnation region under inflow disturbances. Theor. Comput. Fluid Dyn. 14, 377–398.

Behnia, M., Parneix, S., Shabany, Y., Durbin, P.A., 1999. Numerical study of turbulent heat transfer in confined and unconfined impinging jets. Int. J. Heat Fluid Flow 20 (1), 1–9.

Beitelmal, A.H., Saad, M.A., Patel, C.D., 2000. The effect of inclination on the heat transfer between a flat surface and an impinging two-dimensional air jet. Int. J. Heat Fluid Flow 21, 156–163.

Cebeci, T., 1973. A model for eddy conductivity and turbulent Prandtl number. ASME J. Heat Trans. 95, 227–236.

Chen, M., Chalupa, R., West, A.C., Modi, V., 2000. High Schmidt mass transfer in a laminar impinging slot jet flow. Int. J. Heat Mass Trans. 43, 3907–3915.

Chou, Y.J., Hung, Y.H., 1994. Impingement cooling of an isothermally heated surface with a confined slot jet. ASME J. Heat Trans. 116, 479–482.

Chung, Y.M., Luo, K.H., Sandham, N.D., Williams, J.J.R., 2001. Direct numerical simulation of an impinging jet. In: Proceedings of the Turbulence and Shear Flow Phenomena-2, Stockholm, Sweden, pp. 271–276.

Didden, N., Ho, C.M., 1985. Unsteady separation in a boundary layer produced by an impinging jet. J. Fluid Mech. 160, 235–256.

Gardon, R., Akfirat, J.C., 1966. Heat transfer characteristics of impinging two-dimensional air jets. ASME J. Heat Trans. 88, 101–108.

Gauntner, J., Livingood, N.B., Hrycak, P., 1970. Survey of literature on flow characteristics of a single turbulent jet impinging on a flat plate. NASA TN D-5652 Lewis Research Center, USA.

Gaviglio, J., 1987. Reynolds analogies and experimental study of heat transfer in the supersonic boundary layer. Int. J. Heat Mass Trans. 30 (5), 911–926.

Ho, C.M., Huerre, P., 1984. Perturbed free shear layers. Ann. Rev. Fluid Mech. 16, 365–424.

Ho, C.M., Nosseir, N.S., 1981. Dynamics of an impinging jet. Part 1. The feedback phenomenon. J. Fluid Mech. 105, 119–142.

Hoffmann, G., Benocci, C., 1994. Numerical simulation of spatially developing planar jets. In: Application of Direct and Large Eddy Simulation to Transition and Turbulence, AGARD-CP-551, pp. 26-1–26-6.

Huang, P.G., Coleman, G.N., Bradshaw, P., 1995. Compressible turbulent channel flows: DNS results and modelling. J. Fluid Mech. 305, 185–218.

Jambunathan, K., Lai, E., Moss, M.A., Button, B.L., 1992. A review of heat transfer data for single circular jet impingement. Int. J. Heat Fluid Flow 13, 106–115.

Jiang, X., Luo, K.H., 2000. Direct numerical simulation of the puffing phenomenon of an axisymmetric thermal plume. Theor. Comput. Fluid Dyn. 14, 55–74.

Law, H.-S., Masliyah, J.H., 1984. Mass transfer due to a confined laminar impinging two-dimensional jet. Int. J. Heat Mass Trans. 27 (4), 529–539.

Lele, S.K., 1992. Compact finite difference schemes with spectral-like resolution. J. Comput. Phys. 103, 16–42.

Lee, X.C., Ma, C.F., Xheng, Q., Zhuang, Y., Tian, Y.Q., 1997. Numerical study of recovery effect and impingement heat transfer with submerged circular jets of large Prandlt number liquid. Int. J. Heat Mass Trans. 40 (11), 2647–2653.

Lin, Z.H., Chou, Y.J., Hung, Y.H., 1997. Heat transfer behaviors of a confined slot jet impingement. Int. J. Heat Mass Trans. 40 (5), 1095–1107.

Liu, T., Sullivan, J.P., 1996. Heat transfer and flow structure in a excited circular impinging jet. Int. J. Heat Mass Trans. 39 (17), 3695–3706.

Livingood, N.B., Hrycak, P., 1973. Impingement heat transfer from turbulent air stream jets to flat plates—a literature survey. NASA TM X-2778 Lewis Research Center, USA.

Luo, K.H., Sandham, N.D., 1997. Direct numerical simulation of supersonic jet flow. J. Engng. Math. 32, 121–142.

Martin, H., 1977. Heat and mass transfer between impinging gas jets and solid surfaces. Adv. Heat Trans. 13, 1–60.

Meola, C., Luca, L., Carlomagno, G.M., 1996. Influence of shear layer dynamics on impingement heat transfer. Exp. Therm. Fluid Sci. 13, 29–37.

Orlandi, P., Jiménez, J., 1994. On the generation of turbulent wall friction. Phys. Fluids 6 (2), 634–641.

Olsson, M., Fuchs, L., 1998. Large eddy simulations of a forced semiconfined circular impinging jet. Phys. Fluids 10 (2), 476–486.

Özdemir, I.B., Whitelaw, J.H., 1992. Impingement of an axisymmetric jet on unheated and heated flat plates. J. Fluid Mech. 240, 503–532.

Park, T.S., Sung, H.J., 2001. Development of a near-wall turbulence model and application to jet impingement heat transfer. Int. J. Heat Fluid Flow 22, 10–18.

Poinsot, T.J., Lele, S.K., 1992. Boundary conditions for direct simulations of compressible viscous flows. J. Comput. Phys. 101, 104–129.

Popiel, C.O., Trass, O., 1991. Visualization of a free and impinging round jet. Exp. Therm. Fluid Sci. 4, 253–264.

Reynolds, O., 1874. On the extent and action of the heating surface for stream boilers. Proc. Manchester Lit. Philos. Soc. 14, 7–12.

Reynolds, W.C., 1975. The prediction of turbulent Prandtl and Schmidt numbers. Int. J. Heat Mass Trans. 18, 1055–1069.

Sparrow, E.M., Wong, T.C., 1975. Impingement transfer coefficients due to initially laminar slot jets. Int. J. Heat Mass Trans. 18, 597–605.

Thompson, K.W., 1987. Time dependent boundary conditions for hyperbolic systems. J. Comput. Phys. 68, 1–24.

Tucker, P.G., 2001. Computation of Unsteady Internal Flows. Kluwer Academic Publishers, Dordrecht.

Viskanta, R., 1993. Heat transfer to impinging isothermal gas and flame jets. Exp. Therm. Fluid Sci. 6, 111–134.

Webb, B., Ma, C.-F., 1995. Single-phase liquid jet impingement heat transfer. Adv. Heat Trans. 26, 105–134.

Williamson, J.H., 1980. Low-storage Runge–Kutta Schemes. J. Comput. Phys. 35, 48–56.